ISSN 1674-1056
http://cpb.iphy.ac.cn
http://iopscience.iop.org/cpb
中国物理 B
Chinese Physics
中国物理 Chinese Physics B

Achieving high-performance multilayer $MoSe_2$ photodetectors by defect engineering

Jintao Hong(洪锦涛), Fengyuan Zhang(张丰源), Zheng Liu(刘峥), Jie Jiang(蒋杰), Zhangting Wu(吴章婷), Peng Zheng(郑鹏), Hui Zheng(郑辉), Liang Zheng(郑梁), Dexuan Huo(霍德璇), Zhenhua Ni(倪振华), and Yang Zhang(张阳)

Citation: Chin. Phys. B, 2021, 30 (**8**): 087801. DOI: 10.1088/1674-1056/abea8b
Journal homepage: http://cpb.iphy.ac.cn; http://iopscience.iop.org/cpb

What follows is a list of articles you may be interested in

Preparation and photoelectric properties of cadmium sulfide quantum dots

Yue Gu(古月), Libin Tang(唐利斌), Xiaopeng Guo(郭小鹏), Jinzhong Xiang(项金钟), Kar Seng Teng, Shu Ping Lau(刘树平)

Chin. Phys. B, 2019, 28 (**4**): 047803. DOI: 10.1088/1674-1056/28/4/047803

Efficient doping modulation of monolayer WS_2 for optoelectronic applications

Xinli Ma(马新莉), Rongjie Zhang(张荣杰), Chunhua An(安春华), Sen Wu(吴森), Xiaodong Hu(胡晓东), Jing Liu(刘晶)

Chin. Phys. B, 2019, 28 (**3**): 037803. DOI: 10.1088/1674-1056/28/3/037803

Strain-modulated excitonic gaps in mono- and bi-layer $MoSe_2$

Jianting Ji(籍建葶), Anmin Zhang(张安民), Tianlong Xia(夏天龙), Po Gao(高坡), Yinghao Jie(揭英昊), Qian Zhang(张倩), Qingming Zhang(张清明)

Chin. Phys. B, 2016, 25 (**7**): 077802. DOI: 10.1088/1674-1056/25/7/077802

First-principles studies of electronic, optical, and mechanical properties of γ-$Bi_2Sn_2O_7$

Chao-Hao Hu(胡朝浩), Xue-Hui Yin(殷学辉), Dian-Hui Wang(王殿辉), Yan Zhong(钟燕), Huai-Ying Zhou(周怀营), Guang-Hui Rao(饶光辉)

Chin. Phys. B, 2016, 25 (**6**): 067801. DOI: 10.1088/1674-1056/25/6/067801

Electrochromic & magnetic properties of electrode materials for lithium ion batteries

Zheng-Fei Guo(郭正飞), Kun Pan(潘坤), Xue-Jin Wang(王学进)

Chin. Phys. B, 2016, 25 (**1**): 017801. DOI: 10.1088/1674-1056/25/1/017801

Achieving high-performance multilayer $MoSe_2$ photodetectors by defect engineering*

Jintao Hong(洪锦涛)[1], Fengyuan Zhang(张丰源)[1], Zheng Liu(刘峥)[2], Jie Jiang(蒋杰)[3], Zhangting Wu(吴章婷)[1,†], Peng Zheng(郑鹏)[1], Hui Zheng(郑辉)[1], Liang Zheng(郑梁)[1], Dexuan Huo(霍德璇)[4], Zhenhua Ni(倪振华)[3], and Yang Zhang(张阳)[1,‡]

[1] *Laboratory for Nanoelectronics and NanoDevices, Department of Electronics Science and Technology, Hangzhou Dianzi University, Hangzhou* 310018, *China*

[2] *Jiangsu Province Special Equipment Safety Supervision and Inspection Institute, Wuxi* 214170, *China*

[3] *School of Physics, Southeast University, Nanjing* 211189, *China*

[4] *Institute of Materials Physics, Hangzhou Dianzi University, Hangzhou* 310018, *China*

(Received 14 December 2020; revised manuscript received 3 February 2021; accepted manuscript online 1 March 2021)

Optoelectronic properties of $MoSe_2$ are modulated by controlled annealing in air. Characterizations by Raman spectroscopy and XPS demonstrate the introduction of oxygen defects. Considerable increase in electron and hole mobilities reveals the highly improved electron and hole transport. Furthermore, the photocurrent is enhanced by nearly four orders of magnitudes under 7 nW laser exposure after annealing. The remarkable enhancement in the photoresponse is attributed to an increase in hole trapping centers and a reduction in resistance. Furthermore, the annealed photodetector shows a fast time response on the order of 10 ms and responsivity of 3×10^4 A/W.

Keywords: $MoSe_2$, oxygen defects, electrical properties, optoelectronic properties

PACS: 78.30.–j, 85.30.Tv, 85.60.Bt, 85.60.Dw **DOI:** 10.1088/1674-1056/abea8b

1. Introduction

Two-dimensional (2D) semiconductor transition metal dichalcogenides (TMDCs) have attracted considerable interest for applications in electronics and optoelectronics due to their superior electrical, optical, and mechanical properties.[1,2] So far, many efforts have been made to develop 2D TMDCs-based photodetectors with an ultrafast response, high responsivity, and broadband response, to broaden the applications of TMDCs to remote sensing, camera imaging, and optical communications.[3–6] However, the performance of TMDCs photodetectors presents a large variation owing to impurities, scatterings, structural defects, and the metal-semiconductor contact.[7,8] High-performance photodetector based on TMDCs, which perform both ultra-fast response and ultra-sensitivity, remains a significant challenge. Therefore, to fabricate high-performance photodetectors, an efficient modulation process should be developed.

Optoelectronic properties of 2D TMDCs can be effectively modulated through defect engineering.[8] Several approaches have been employed to achieve high-performance TMDC photodetectors, such as oxygen plasma treatment, surface charge transfer doping, ozone exposure, and focused laser beam treatment.[9–12] The enhancement of optoelectronic properties can be mainly attributed to the photogating effect, modulation of trap states, and reduction of Schottky barriers.[9–12] However, there are still some significant concerns about modulation methods of defect engineering. The structure of TMDCs can be damaged by oxygen plasma treatment, resulting in the formation of different types of defects (traps and recombination centers).[9] Carrier recombination and shallow traps improve the response speed and show short response time, while the deep traps prolong response time.[13] For ozone exposure, the formation of self-limiting surface oxides, which serve as effective traps, leads to photogating of the underlying TMDCs. The charge transfer and trapping process of the photogating effect can be in the timescale of millisecond or seconds and gives rise to the ultra-high gain. Recent studies have shown that the high responsivities of ReS_2 and WSe_2 transistors are accompanied by a slow response on the timescale of seconds after oxygen plasma treatment and ozone exposure, respectively.

Here, we report a high-performance $MoSe_2$ photodetector with both a high responsivity of 3×10^4 A/W and fast temporal response on the order of 10 ms, which is achieved by an air annealing technique. The photocurrent of $MoSe_2$ is enhanced by near four orders of magnitudes under 7 nW laser exposure after annealing due to an increase in hole trapping centers and a reduction in resistance.

*Project supported by the National Natural Science Foundation of China (Grant No. 61904043) and the Natural Science Foundation of Zhejiang Province, China (Grant No. LQ19A040009).

†Corresponding author. E-mail: wuzhangting@hdu.edu.cn

‡Corresponding author. E-mail: yzhang09@hdu.edu.cn

© 2021 Chinese Physical Society and IOP Publishing Ltd

2. Methods

Multilayer $MoSe_2$ flakes were prepared by mechanical exfoliation of bulk crystals and then deposited on 285 nm SiO_2/Si substrates. The Raman spectra characterizations were measured using a LabRAM HR800 Raman system with 532 nm excitation laser. The laser spot size was about 2 μm by using a 50× objective lens. X-ray photoelectron spectroscopy (XPS) was taken using thermalfisher ESCALAB 250Xi. The $MoSe_2$ devices were fabricated by transferring the Au electrodes.[14] The $MoSe_2$ device was annealed at 135 °C under argon gas atmosphere for two hours to improve the contacts, as shown in Fig. S1 in the supporting information.[14,15] Then, devices were annealed at different temperatures (50,100, 150, 200, 250, and 300 °C) for one hour (1 h) under air atmosphere to introduce oxygen defects. Electrical and photoresponse characteristics were measured using a Keithley 4200A-SCS parameter analyzer in the atmosphere environment. A laser at wavelength of 532 nm was employed to attain optoelectronic properties.

3. Results and discussion

In order to investigate the effects of air annealing on the $MoSe_2$, we first performed Raman spectroscopy and XPS analyses on $MoSe_2$ films. Fig. 1(a) presents the evolution of Raman spectra for multilayer $MoSe_2$ before and after air annealing treatment at 250 °C and 300 °C, respectively. For pristine multilayer $MoSe_2$, two distinctive Raman modes are observed, the out-of-plane A_{1g} mode (240.1 cm^{-1}) and the in-plane E^1_{2g} mode (283.7 cm^{-1}).[16,17] The peak position of A_{1g} mode is sensitive to the number of layers and doping, while the E^1_{2g} mode is sensitive to strain.[17–20] We then extracted the Raman peak shift values in the two peaks as a function of temperature (Fig. 1(b)). In the case of A_{1g} mode, blue-shifting (0.8 cm^{-1}) is observed after air annealing, indicating that air annealing causes the stiffening of vibrational mode. Figure 1(c) presents the zoom-in Raman spectra in the range around E^1_{2g} mode. Compared with the pristine sample, the E^1_{2g} mode position shows a little red-shifting (0.3 cm^{-1}), which indicates that strain may be induced by air annealing. The Raman spectra of monolayer $MoSe_2$ in Fig. 1(d) indicate that there is blue-shift (0.7 cm^{-1}) in the peak position of A_{1g} mode, and no layer thinning is induced during the air annealing process. The blue-shift of A_{1g} mode can be attributed to the charge transfer induced p-type doping caused by air annealing.[18,19] Vacancy defects of $MoSe_2$ contain dangling bonds, which are active centers for molecular adsorption. Therefore, O_2 can be considered as chemisorbed on the vacancy defects with much stronger binding energy and introduce p-type doping during the air annealing process.[19] XPS is used to study the change of $MoSe_2$ structure after air annealing. Here, a bulk sample is used due to experimental limitations. The XPS spectra of pristine and 250 °C annealed $MoSe_2$ are shown in Figs. 1(e) and 1(f). For pristine $MoSe_2$, the doublet peaks at 229.5 and 232.6 eV correspond to $Mo^{4+}3d_{5/2}$ and $Mo^{4+}3d_{3/2}$. After annealing, additional doublet peaks are located at 232.5 and 235.6 eV belonging to $Mo^{6+}3d_{5/2}$ and $Mo^{6+}3d_{3/2}$, indicating the existence of oxygen defects, such as MoO_x.[16] The increase of charge transfer between oxygen defects and $MoSe_2$ induces p-type doping.

To characterize the air annealing effects on the electrical performance of multilayer $MoSe_2$ FETs, we then fabricated back-gated $MoSe_2$ FET devices and performed current-voltage measurements (I_{DS}–V_{GS} and I_{DS}–V_{DS}) under an ambient environment. At the given V_{DS} of 0.2 V, the transfer curves (I_{DS}–V_{GS}) of $MoSe_2$ FET (channel length is 10 μm and width is 8 μm) before and after annealing at different temperatures are presented in Fig. 2(a). The pristine device indicates a typical n-type conductance behavior. It has been known that chalcogen vacancies result in n-type doping of transition metal dichalcogenides.[10,21–23] With the introduction of oxygen defects, the p-type doping leads to the lowering of Fermi level, and the hole transport is observed. After annealing at 250 °C, the transfer curve becomes ambipolar with a higher electron current level. The minimum conductivity point is moving to the positive direction of gate voltage. The ambipolar behavior of $MoSe_2$ FET is due to its relatively smaller bandgap and the introduction of high-concentration oxygen defects. Figure 2(b) shows the shift of threshold voltage (ΔV_{TH}) with respect to the value for the pristine curve and electron concentration as a function of annealing temperature. The electron concentration is estimated by $n_e = q^{-1}C_g|V_{TH}|$, where $q = 1.6\times10^{-19}$ C, V_{TH} is threshold voltage, and $C_g = 1.15\times10^{-8}$ F·cm^{-2} for the 300-nm-thick SiO_2 layer.[24] According to the formula $\Delta n_e = q^{-1}C_g|\Delta V_{TH}|$, the decrease of electron concentration in the $MoSe_2$ layer with $\Delta V_{TH} = 42.8$ V is about 3.0×10^{12} cm^{-2} after annealing at 250 °C, which indicates that the electrons in the pristine $MoSe_2$ are removed, and annealing in air leads to p-type doping.

Figure 2(c) shows the field-effect mobility of holes and electrons versus temperature. The field-effect mobility of the multilayer $MoSe_2$ is evaluated by $\mu = \frac{L}{WC_gV_{DS}}\frac{\partial I_{DS}}{\partial V_{GS}}$, where $\partial I_{DS}/\partial V_{GS}$ represents the maximum slope extracted from the linear region of the transfer curves, and L and W are the length and the width of the conduction channel, respectively. The electron mobility of the device increases from 7.69 cm^2/V·s to 28.73 cm^2/V·s after annealing in air at 250 °C, revealing the improved electron transport in the $MoSe_2$ channel due to the formation of oxygen defects. The chalcogen vacancies can be partially repaired by oxygen defects during annealing, resulting in the reduction of localized states in the bandgap and improvement of mobility.[25,26] The hole mobility is calculated to be 21.43 cm^2/V·s after annealing at 250 °C. The output curves (I_{DS}–V_{DS}) of the same device at $V_{GS} = 0$ V are shown in

Fig. 2(d) before and after annealing at 250 °C. The nonlinear I_{DS} of pristine $MoSe_2$ versus V_{DS} indicates Schottky barriers (SBs) for electron transport at the metal/$MoSe_2$ interface. In contrast, higher current and more ohmic contact behavior are observed for the annealed device due to repairment of vacancies and reduction in SBs. Therefore, the improved performance of $MoSe_2$ FET can be attributed to the reduction of vacancies and reduction in contact resistance induced by oxygen defects. Threshold voltage and electron mobility distributions of pristine multilayer $MoSe_2$ FETs and these devices after annealing in air at 250 °C are plotted in Figs. S2(a) and S2(b). Figure S3 presents transfer curves of these devices before and after annealing. The annealed $MoSe_2$ devices possess mobilities and threshold voltages much higher than those of the pristine FETs. However, after further increasing the temperature to 300 °C, the I_{DS} drops as shown in Fig. S4, which illustrates that $MoSe_2$ FET begins to be damaged. Under such a high temperature in air, other types of structural defects, such as cracks,[19,27] can be introduced into the $MoSe_2$.

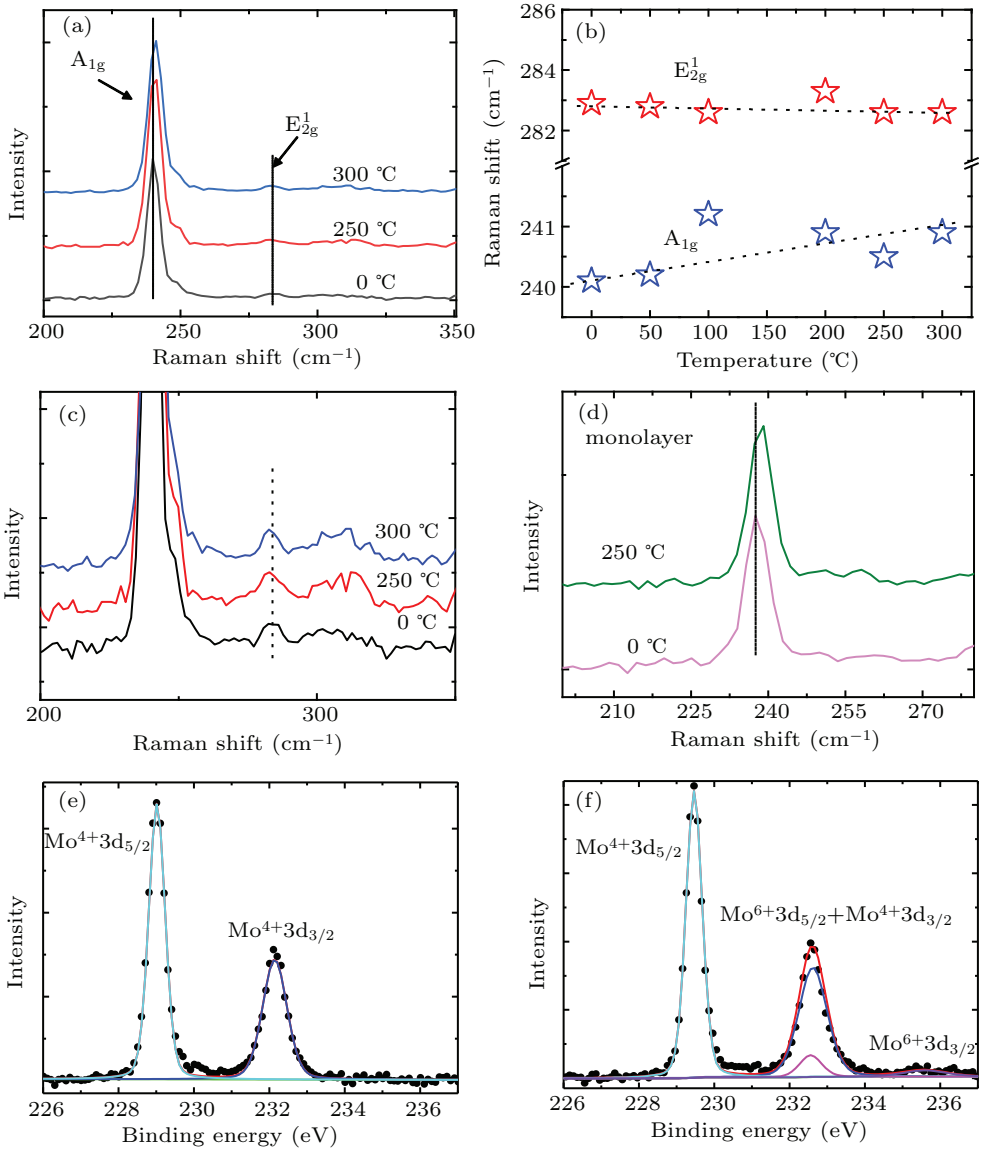


Fig. 1. (a) Raman spectra of multilayer $MoSe_2$ before and after annealing in air for 1 h at 250 °C and 300 °C. (b) Position of A_{1g} and E^1_{2g} as a function of temperature. (c) The zoom-in Raman spectra in the range around E^1_{2g} mode. (d) Raman spectra of monolayer $MoSe_2$ before and after annealing in air for 1 h at 250 °C. (e) and (f) XPS spectra of the original and annealed $MoSe_2$ at 250 °C.

Next, we further evaluated the photoresponse characteristics at $V_{DS} = 1$ V and $V_{GS} = 0$ V of the $MoSe_2$ phototransistor before and after annealing in air at 250 °C, which were recorded with laser-focused on the device at a wavelength of 532 nm (spot size ~ 2 μm). Figures 3(a) and 3(c) show the photoresponse of pristine and annealed device under different laser powers, where positive photocurrents ($I_{ph} = I_{light} - I_{dark}$, with I_{dark} and I_{light} being channel currents under dark and laser illumination) are observed under laser irradiation. Especially, the photocurrent increases significantly, e.g., by nearly three orders of magnitude from 0.4 nA to 438 nA under the same laser power after annealing for 1 h at 250 °C, as shown

in Fig. 3(b). The photocurrent of $MoSe_2$ phototransistor after annealing is large enough for direct measurement without any amplifier, even at a very low laser power (~ 0.22 pW). The detection limit of the pristine device is at ~ 7 nW. Figure 3(d) presents the photocurrent versus V_{DS} under different laser powers. A linear dependence of the photocurrent implies that photoresponse can be effectively tuned by V_{DS}, which is an attractive feature for imaging applications. The remarkable enhancement in the photoresponse is proposed to arise from an increase in hole trapping centers and a reduction in contact resistance. After annealing, electrons transfer from $MoSe_2$ to oxygen defects.[19] Then, electrons are localized at the oxygen defects, inducing a positive depletion layer in $MoSe_2$ near the oxygen defects/$MoSe_2$ interface and the formation of built-in electric field. The photogenerated electron-hole pairs in $MoSe_2$ will be separated by built-in electric field: electrons diffuse toward multilayer $MoSe_2$, while holes accumulate at the oxygen defects/$MoSe_2$ interface.

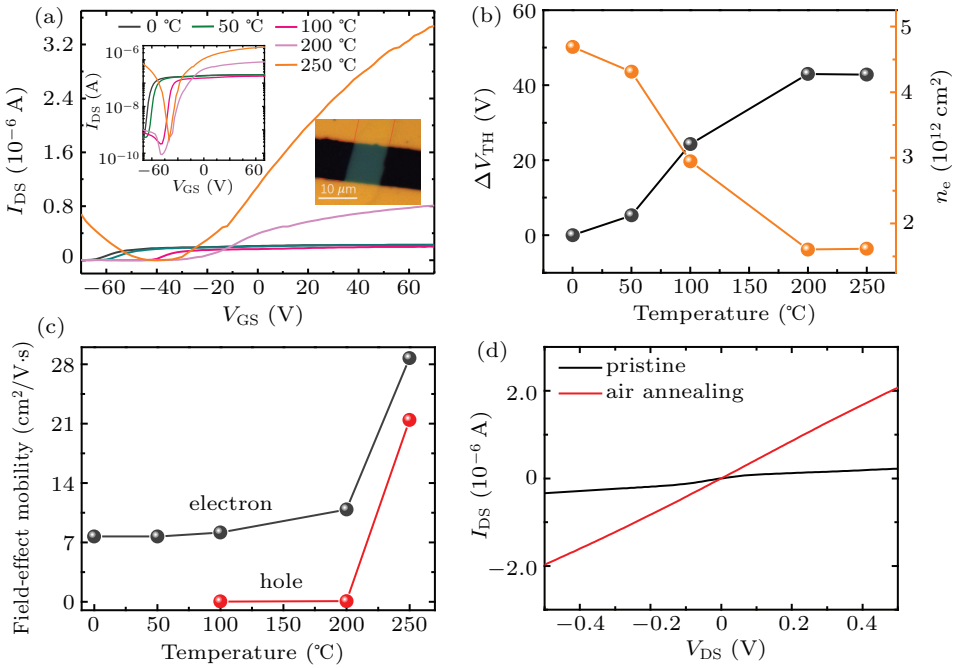


Fig. 2. (a) I_{DS}–V_{GS} curves of $MoSe_2$ FET before and after annealing at different temperatures. Inset: I_{DS}–V_{GS} curves on a logarithmic scale. (b) Shift of threshold voltage (ΔV_{TH}) and electron concentration (n_e) as a function of temperature. (c) The field-effect mobility (μ) of holes and electrons as a function of temperature. (d) I_{DS}–V_{DS} curves of $MoSe_2$ FET before and after annealing in air.

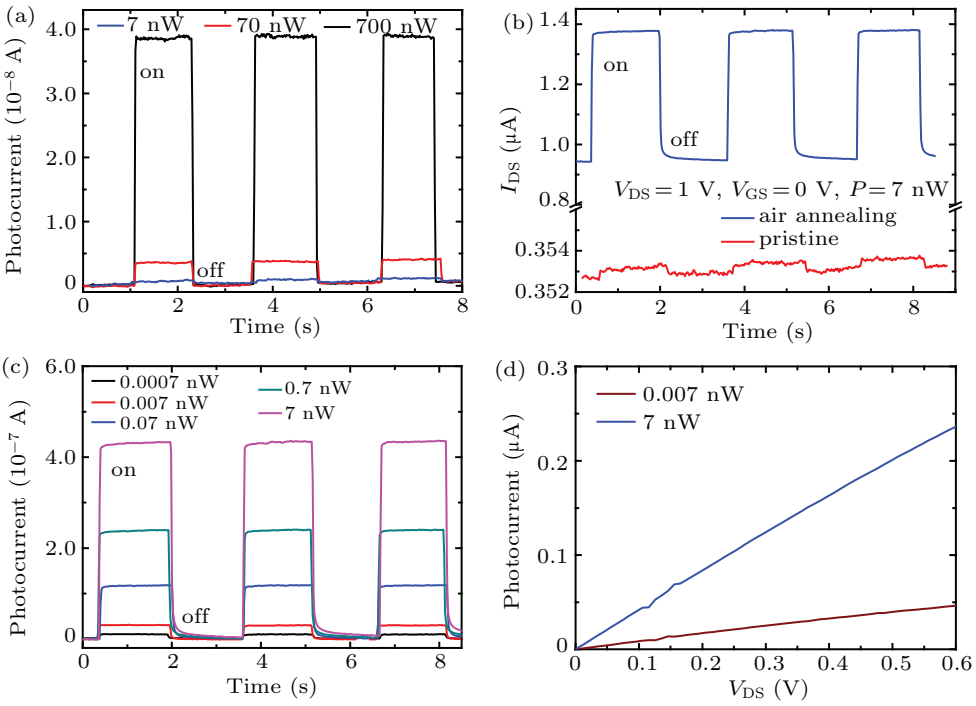


Fig. 3. Photoresponse of pristine (a) and annealed (c) $MoSe_2$ device under different laser power. (b) Photoresponse of pristine and annealed $MoSe_2$ device under 7 nW laser power. (d) Photocurrent evolution with V_{DS} at different laser powers.

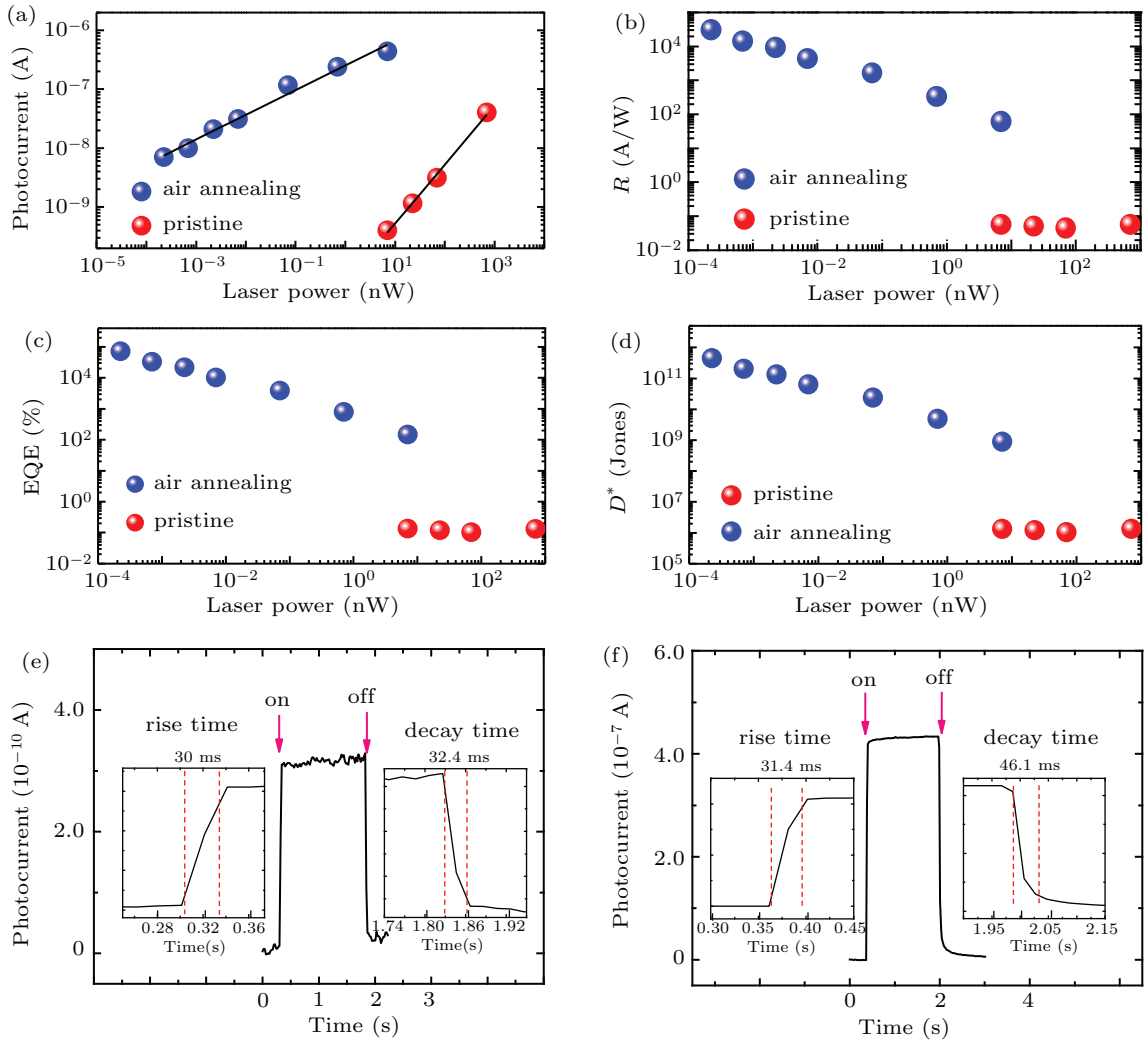


Fig. 4. (a)–(d) Photocurrent, R, EQE, and D^* of the $MoSe_2$ phototransistor as a function of incident power before and after annealing. (e) and (f) The temporal photoresponse characteristic of the $MoSe_2$ phototransistor before and after annealing. The corresponding rise and decay process are indicated in the inset.

Therefore, oxygen defects can be treated as hole localization centers under illumination and result in the photogating effect. By applying V_{DS}, photogenerated electrons drift and recirculate in the $MoSe_2$ channel before recombining with the holes, leading to the high gain of the device.[7] The increase of electron density and high positive photocurrents in $MoSe_2$ are achieved. Also, reduction in contact resistance facilitates the transport of the photo-induced charge carriers, leading to an enhancement in the photocurrent.

The power-law ($I_{ph} \sim P^{\alpha}$) fits the power-dependent photoresponse (Fig. 4(a)), where I_{ph} is the net photocurrent, P is the effective illuminated power of the device.[28,29] The photocurrent of the annealed device has a sublinear relationship ($\alpha = 0.42$) with the laser power and saturates at high power, while that of the pristine device ($\alpha = 0.99$) continues to increase with laser power. The localization of photogenerated holes at the oxygen defects/$MoSe_2$ interface leads to a reversed electric field to balance the equilibrium built-in field. Therefore, fewer photogenerated electron-hole pairs will be separated in the annealed device due to the weaker built-in field under higher laser power. The photocurrent of the pristine device increases almost linearly with laser power, demonstrating that the efficiency of electron-hole pair generations is almost proportional to the absorbed photon flux.[30] Furthermore, the carrier recombination is dominated by the Shockley–Read–Hall process via the large trap states in pristine $MoSe_2$.[28] The responsivity (R) of the device under different laser powers before and after annealing is shown in Fig. 4(b), which is defined as $R = I_{ph}/PS$ in units of A/W, where I_{ph} is the photocurrent, P is the incident light power density, and S is the active area. After annealing, the responsivity reaches a value as high as 3×10^4 A/W at laser power of 0.22 pW. Based on the value of R, the external quantum efficiency (EQE) under different laser powers is estimated, as shown in Fig. 4(c). EQE is the ratio between the number of electron-hole pairs contributed to the photocurrent and the number of incident photons.[7] EQE of the annealed device is as high as $7.8 \times 10^6\%$ at laser power of 0.22 pW, which can be attributed to the reduction of carrier recombination before being collected by the electrodes.[7] Besides the EQE recorded, another key feature for sensitive pho-

todetection is the detectivity (D^*), which is defined as $D^* = A^{1/2}R/(2eI_d)^{1/2}$, where R is the responsivity, A is the area of the detector, e is the unit of charge, and I_d is the dark current. The calculated D^* of the device as a function of incident laser power is shown in Fig. 4(d). The D^* is greatly enhanced from 1.3×10^6 Jones to 9.0×10^8 Jones at a laser power of 7 nW due to the great increase of photocurrent after annealing in air. At a low laser power of 2 pW, D^* is higher than 10^{11} Jones. This high D^* results from the highly efficient charge separation and large photoconductive gain.[31] Figures 4(e) and 4(f) present the temporal photoresponse characteristics of the $MoSe_2$ phototransistor before and after annealing. The rising (τ_r) and decaying (τ_d) times extracted between 10% and 90% of the increasing and decreasing photocurrents are estimated to be 30 ms and 32.4 ms for the pristine device, respectively. After annealing, the photoresponse times slightly increase (τ_r: 30→31.4 ms and τ_d: 32.4→46.1 ms). Such a fast speed is superior to other TMDCs-based photoconductors with the photogating mechanism.[30,32–34]

4. Conclusion and perspectives

In summary, we have demonstrated a significant enhancement in the photodetection performance of $MoSe_2$ phototransistor after air annealing. Characterizations by Raman spectroscopy and x-ray photoelectron spectroscopy (XPS) reveal the introduction of oxygen defects and the hole doping effect. Both electron and hole mobilities are considerably increased, revealing the highly improved electron and hole transport in the $MoSe_2$ channel. In addition, the photocurrent of $MoSe_2$ is also enhanced by nearly four orders of magnitudes under 7 nW laser exposure after annealing in air. The annealed photodetector shows a responsivity of 3×10^4 A/W, EQE of 7.8×10^6%, and detectivity of 4.5×10^{11} Jones. Especially, the photodetector presents a fast time response on the order of 10 ms after air annealing. The present study provides a valuable route of fabricating high-performance 2D nanodevices for electronic and optoelectronic applications.

References

[1] Mak K F and Shan J 2016 *Nat. Photon.* **10** 216
[2] Dai Z H, Liu L Q and Zhang Z 2019 *Adv. Mater.* **31** 1805417
[3] Wang L, Liu C L, Chen X S, Zhou J, Hu W D, Wang X F, Li J H, Tang W W, Yu A Q, Wang S W and Lu W 2017 *Adv. Funct. Mater.* **27** 1604414
[4] Miao J S, Song B, Xu Z H, Cai L, Zhang S M, Dong L X and Wang C 2017 *Small* **14** 1702082
[5] Ye Y, Wong Z J, Lu X F, Ni X J, Zhu H Y, Chen X H, Wang Y and Zhang X 2015 *Nat. Photon.* **9** 733
[6] Xie C, Mak C, Tao X M and Yan F 2016 *Adv. Funct. Mater.* **27** 1603886
[7] Tu L Q, Cao R R, Wang X D, Chen Y, Wu S Q, Wang F, Wang Z, Shen H, Lin T, Zhou P, Meng X J, Hu W D, Liu Q, Wang J L, Liu M and Chu J H. 2020 *Nat. Commun.* **11** 101
[8] Hu Z H, Wu Z T, Han C, He J, Ni Z H and Chen W 2018 *Chem. Soc. Rev.* **47** 3100
[9] Shim J, Oh A, Kang D H, Oh S, Jang S K, Jeon J, Jeon M H, Kim M, Choi C, Lee J, Lee S, Yeom G Y, Song Y J and Park J H 2016 *Adv. Mater.* **28** 6985
[10] Jo S H, Kang D H, Shim J, Jeon J, Jeon M H, Yoo G, Kim J, Lee J, Yeom G Y, Lee S, Yu H Y, Choi C and Park J H 2016 *Adv. Mater.* **28** 4824
[11] Lu J P, Carvalho A, Chan X K, Liu H W, Liu B, Tok E S, Loh K P, Castro Neto A H and Sow C 2015 *Nano Lett.* **15** 3524
[12] Yamamoto M, Ueno K and Tsukagoshi K 2018 *Appl. Phys. Lett.* **112** 181902
[13] Jiang J, Ling C Y, Xu T, Wang W H, Niu X H, Zafar A, Yan Z Z, Wang X M, You Y M, Sun L T, Lu J P, Wang J L and Ni Z H 2018 *Adv. Mater.* **30** 1804332
[14] Wu Z T, Luo Z Z, Shen Y Y, Zhao W W, Wang W, Nan H Y, Guo X T, Sun L T, Wang X R, You Y M and Ni Z H 2016 *Nano Res.* **9** 3622
[15] Long M S, Wang Y, Wang P, Zhou X H, Xia H, Luo C, Huang S Y, Zhang G W, Yan H G, Fan Z Y, Wu X, Chen X S, Lu W and Hu W D 2019 *ACS Nano* **13** 2511
[16] Chen X S, Liu G B, Hu Y X, Cao W W, Hu P A and Hu W P 2017 *Nanotechnology* **29** 045202
[17] Tonndorf P, Schmidt R, Böttger P, Zhang X, Börner J, Liebig A, Albrecht M, Kloc C, Gordan O, Zahn D R T, Vasconcellos S M de and Bratschitsch R 2013 *Opt. Express* **21** 4908
[18] Zheng X M, Wei Y H, Liu J X, Wang S T, Shi J, Yang H, Peng G, Deng C Y, Luo W, Zhao Y, Li Y Z, Sun K, Wan W, Xie H P, Gao Y L, Zhang X A and Huang H 2019 *Nanoscale* **11** 13469
[19] Nan H Y, Wang Z L, Wang W H, Liang Z, Lu Y, Chen Q, He D W, Tan P H, Miao F, Wang X R, Wang J and Ni Z H 2014 *ACS Nano* **8** 5738
[20] Conley H J, Wang B, Ziegler J I, Haglund R F, Pantelides S T and Bolotin K I 2013 *Nano Lett.* **13** 3626
[21] Zhang X K, Liao Q L, Liu S, Kang Z, Zhang Z, Du J L, Li F, Zhang S H, Xiao J K, Liu B S, Ou Y, Liu X Z, Gu L and Zhang Y 2017 *Nat. Commun.* **8** 15881
[22] Jiang J, Xu T, Lu J P, Sun L T and Ni Z H 2019 *Research* **2019** 4641739
[23] Wang Z, Wang P, Wang F, *et al*. 2019 *Adv. Funct. Mater.* **30** 1907945
[24] Wu Z T, Zhu N C, Jiang J, Zafar A, Hong J T and Zhang Y 2019 *APL Mater.* **7** 041108
[25] Nan H Y, Wu Z T, Jiang J, Zafer A, You Y and Ni Z H 2017 *J. Phys. D: Appl. Phys.* **50** 154001
[26] Yu Z H, Pan Y M, Shen Y T, Wang Z L, Ong Z Y, Xu T, Xin R, Pan L J, Wang B G, Sun L T, Wang J L, Zhang G, Zhang Y W, Shi Y and Wang X R 2014 *Nat. Commun.* **5** 5290
[27] Liu B L, Ma Y Q, Zhang A Y, Chen L, Abbas A N, Liu Y H, Shen C F, Wan H C and Zhou C W 2016 *ACS Nano* **10** 5153
[28] Wu G J, Wang X D, Chen Y, Wu S Q, Wu B M, Jiang Y Y, Shen H, Lin T, Liu Q, Wang X R, Zhou P, Zhang S T, Hu W, Meng X J, Chu J H and Wang J L 2020 *Adv. Mater.* **32** 1907937
[29] Wang Y, Wu P S, Wang Z, *et al*. 2020 *Adv. Mater.* **32** 2005037
[30] Zhang W J, Chiu M H, Chen C H, Chen W, Li L J and Wee A T S 2014 *ACS Nano* **8** 8653
[31] Huo N J and Konstantatos G 2017 *Nat. Commun.* **8** 572
[32] Kufer D, Nikitskiy L, Lasanta T, Navickaite G, Koppens F H L and Konstantatos G 2014 *Adv. Mater.* **27** 176
[33] Hu C, Dong D D, Yang X K, Qiao K, Yang D, Deng H, Yuan S J, Khan J, Lan Y, Song H S and Tang J 2016 *Adv. Funct. Mater.* **27** 1603605
[34] Hu Z H, Li Q, Lei B, Wu J, Zhou Q H, Gu C D, Wen X L, Wang J Y, Liu Y P, Li S S, Zheng Y, Lu J P, He J, Wang L, Xiong Q H, Wang J L and Chen W 2018 *Adv. Mater.* **30** 1801931